A VIRTUAL TEST-BED FOR THE PREDICTION OF HOLISTIC EFFECTIVE ELASTIC PROPERTIES OF UD COMPOSITES

A. I. Akpoyomare[1] *, M. I. Okereke[1]
[1] Department of Systems Engineering, University of Greenwich, Kent, UK, ME4 4TB.
* Corresponding author (a.i.akpoyomare@gre.ac.uk)

Keywords: *Effective elastic properties, finite element analysis (FEA), boundary conditions, virtual testing, homogenization, fibre reinforced composites, 3D representative volume elements*

Abstract

Most existing computational approaches are restrictive in their predictive capabilities by using non-representative virtual geometric domains (RVEs) of test materials. The strategy proposed here relaxes these restrictions by utilizing statistically representative 3D RVEs with appropriate boundary conditions and a robust homogenization implementation based on a micromechanical modelling philosophy. The strategy was implemented as a self-consistent, rigorous, virtual testing framework analogous to a physical experimental testing scheme. The strategy proposed in this work was shown to give a holistic set of elastic properties of the test composites considered when compared with other predictive approaches. Also, parametric studies were carried out to explore the different features of the virtual framework. Therefore, this virtual test-bed strategy represents a suitable substitute for realistic experiments and can be used in designing different virtual experiments.

1. Introduction

A prerequisite for any virtual testing scheme is the generation of appropriate virtual geometric domains, which are inherently characteristic of the test composites under investigation. Such domains are commonly described as representative volume elements (RVEs). Numerical algorithms used to generate these RVEs for composite materials assume either deterministic (i.e. Square or Hexagonal) or random spatial configurations of reinforcements within the matrix medium. Using a combined numerical-statistical method, Trias and co-workers [1] showed that the difference in predicted effective Young's modulus and Poisson's ratio between both assumptions, for the material they considered, was 12% and 2% respectively. Furthermore, the authors established that deterministic models significantly underestimated damage initiation variables. Hence, RVEs with random spatial configurations of reinforcements are crucial for accurate numerical analyses.

Moreover, most existing virtual testing schemes for unidirectional (UD) composites often approximate 3D problems with 2D models. This is generally motivated by the need to simplify models to ensure less computational demands. However, such models are limited in their predictive capacity. For example, such models often predict only four, out of five independent, elastic constants i.e. E_{22}, E_{33}, G_{23} and v_{23} (with the 1-axis representing the fibre-axis); and E_{11} is usually obtained from crude estimates based on the rule of mixtures [2]. Comparative analyses of 2D and 3D model predictions of de-bonding in composite skin-stiffened panels showed appreciable differences between predictions using both methods [3]. The authors concluded that whilst 2D approximations are less computationally demanding, they should only be used qualitatively and 3D RVEs should be deployed when accurate quantitative predictions are required.

A seminal work adopting 3D RVEs to predict the effective elastic properties of UD composites is that of Sun and Vaidya [4]. However, the authors utilised deterministic arrangements of reinforcements within generated RVEs, although, their predictions agreed quite well with experimental data. Nevertheless, their methodology for imposing periodic boundary conditions (PBCs) made restrictive assumptions about the deformation of the test composite along the fibre axis. This approach requires a priori knowledge of the material response along the fibre axis, which violates the fundamental principle of developing a virtual testing framework devoid of overly restrictive assumptions about the constitutive response of test materials.

Recently, Melro and associates [5] statistically investigated the influence of several different geometric parameters on the effective elastic response of UD composites. Their work was based on 3D RVEs with a random spatial arrangement of fibres along the transverse direction of the RVE, prescribed with PBCs. The geometric parameters considered were the fibre radius, dimensions of the RVE, and minimum distance between neighbouring fibres within the RVEs. The authors postulated that utilizing 3D RVEs with a random spatial configuration of fibres, in conjunction with a system of imposing PBCs, and numerically/statistically determining the effect of certain geometric parameters, constitutes a road-map for performing

high-fidelity micromechanical computational analysis on UD composites.

Therefore, in lieu of the foregoing thesis presented by several authors, this communication presents a robust virtual framework based on 3D RVEs, capable of accurately predicting the holistic elastic response of UD composites. The methodology presented here is based solely on knowledge of the properties of constituent phases (i.e. fibre/matrix) comprising the test material. Most importantly, there were no assumptions regarding a prior knowledge of material constitutive response in any material test direction.

In the following sections, details of the proposed virtual framework are espoused.

2. The virtual test-bed

The proposed virtual test-bed comprises a multi-step implementation process ranging from the development/isolation of appropriate RVEs of test materials, to the determination of their effective elastic properties. Fig. 1 shows a schematic rendition of the key component steps within the test-bed.

2.1. Generation of virtual geometric domains (RVEs)

Micromechanical analyses of materials mandates the determination of well-defined RVEs [6]. An intrinsic feature of manufactured composites is the presence of an interphase region between the fibres and matrix. However, for the purpose of this study, perfect bonding between the fibres and the matrix was assumed.

2.1.1. Virtual 2D geometric modelling

In this study, a geometric modelling algorithm, *Monte Carlo RVE Generator* (*MCRVEGen*), was developed to automate the generation of virtual domains for composites with pseudo-randomly positioned inclusions. The *MCRVEGen* algorithm was developed based on expositions from the Hard-Core Model [7]. Essentially, the *MCRVEGen* algorithm iteratively populates a pre-defined 2D virtual domain, which represents the cross-section of a given UD test material, with randomly positioned non-intersecting circles, representing the reinforcing fibres, until a required volume fraction is attained. The *MCRVEGen* algorithm comprises two principal modules: (i) the Hard-Core Model module, and (ii) the application of periodicity of material constraints module.

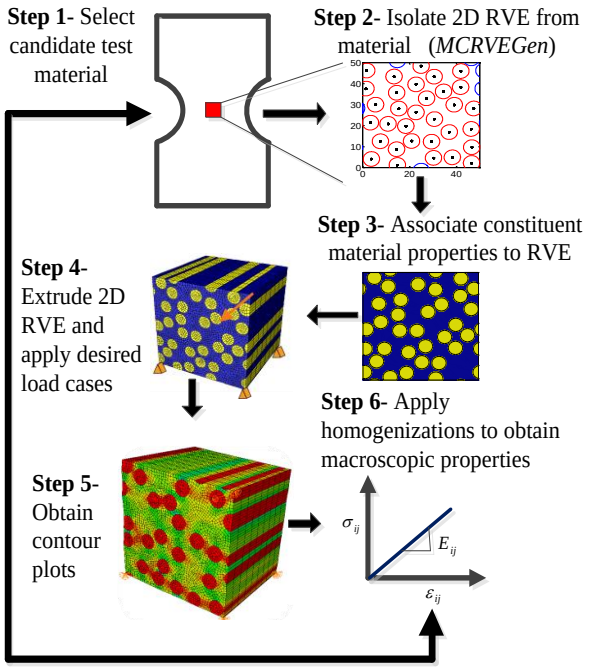

Fig. 1. Schematic of the multi-step implementation of the virtual test-bed.

2.1.2. Preventing fibre overlap within virtual domain

Pseudo-randomly positioned inclusions within a virtual domain are liable to intersections; hence, the need for a strategy to prevent such non-physical phenomenon.

Consider Fig. 2 which shows a schematic of the cross-section of a typical RVE domain with randomly positioned inclusions. The coordinates of the origin of this domain is defined as $\{X_{0RVE}, Y_{0RVE}\}$; likewise, a point diagonal to the origin is defined as $\{X_{LRVE}, Y_{HRVE}\}$, where L_{RVE} and H_{RVE} represent the width and height of the RVE domain respectively. Also, assume there exists an *i*-th fibre within this domain, with coordinates defined as $\{X_i, Y_i\}$ and a diameter, $\emptyset_i$. If the distance between this fibre and any other fibre within this domain is designated as d_n, where $n = 1, 2, 3 \ldots i-1$,this fibre may be considered to overlap, if and only if, $d_n < \emptyset_i$. The distance d_n is evaluated based on equation 1.

$$d_n = \sqrt{(X_n - X_i)^2 + (Y_n - Y_i)^2} \tag{1}$$

The *MCRVEGen* algorithm enforces the condition, $d_n \leq \beta\emptyset_i$; where β represents a scalar coefficient with the following condition: $\beta \geq 1$. Within the context of this study, the authors

enforced $\beta > 1$ to avoid fibre contiguity within the virtual domain.

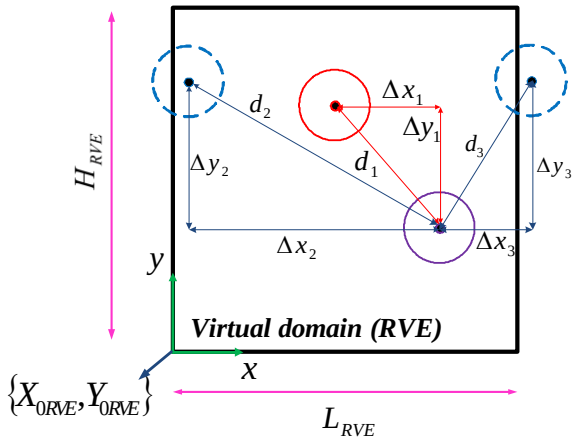

Fig. 2. Methodology for preventing fibre intersections within virtual domain.

2.1.3. Periodicity of material constraint

Periodicity of material constraints require the complementary fraction of boundary penetrating inclusions to reappear on the corresponding side of the RVE. This condition is mandatory in order to ensure stress continuity across the boundaries of the RVE; thereby, precluding wall-effects [6]. Hence, in developing *MCRVEGen*, an approach for detecting and eliminating wall-effects was developed.

Again, consider Fig. 3 which depicts an RVE enforced with the periodicity of material constraints. Here, the coordinates and dimensions of the RVE and fibres retain their previous definitions used earlier within this paper (i.e. $\{X_{0RVE}, Y_{0RVE}\}$ etc.). Assuming an *i*-th boundary penetrating fibre exists within the window, three distinct categories of boundary penetration for this fibre are possible: X-axis, Y-axis and corner/vertex categories respectively. An *i*-th boundary penetrating fibre is said to satisfy any of these categories if either of the following expressions is satisfied.

(a) $|X_i - X_{0RVE}| < 0.5\emptyset_i$ or $|X_i - X_{LRVE}| < 0.5\emptyset_i$ for X-axis boundary penetrating fibres,
(b) $|Y_i - Y_{0RVE}| < 0.5\emptyset_i$ or $|Y_i - Y_{LRVE}| < 0.5\emptyset_i$ for Y-axis boundary penetrating fibres
(c) $|X_i - X_{0RVE}| < 0.5\emptyset_i$ and $|Y_i - Y_{LRVE}| < 0.5\emptyset_i$ for boundary fibres close to the origin of the virtual domain; $|X_i - X_{LRVE}| < 0.5\emptyset_i$ and $|Y_i - Y_{HRVE}| < 0.5\emptyset_i$ for boundary fibres close to the diagonal of the origin or the RVE.

The preceding arguments defining boundary fibre penetration can be extended to the other vertices of the RVE domain.

2.1.4. Spatial characterization of generated RVEs

Having developed a scheme for generating 2D virtual domains, it becomes imperative to assess the 'appropriateness' of these domains in describing actual test materials. Two important criteria are generally used in performing this assessment: (a) the thermo-mechanical conformations of the RVEs, and (b) the spatial distributions of inclusions within the RVE. The latter is accomplished by using appropriate statistical spatial descriptors which include, Voronoi polygon areas, neighbouring fibre distances, nearest neighbour distances, nearest neighbour orientations, Ripley's K function and Pair distribution functions [8]. In this study, the nearest neighbour distance was adopted. This statistic was obtained using a Probability Density Function (PDF) of proximity interactions between a given fibre and its nearest neighbours. This statistical measure is particularly sensitive to point (reinforcement) agglomeration within any given domain; therefore, it is imperative that this characteristic be reproduced faithfully as particle agglomeration can be a precursor to damage initiation sites [1]. A digitized micrograph was created from a random regional sample of a typical glass-fibre UD reinforced polypropylene, *Plytron*™. The statistical descriptor of this digitized sample was compared against several RVEs generated using *MCRVEGen* as shown in Fig. 5. The results show the *MCRVEGen* RVEs are representative of typical samples of UD composites. Fig.4 shows typical RVEs generated using the *MCRVEGen* algorithm.

2.1.5. Generation of 3D virtual domains

3D RVEs were obtained by extruding *MCRVEGen*-based 2D RVEs within ABAQUS CAE software. Data from *MCRVEGen* were supplied to ABAQUS using a dedicated Python script for this purpose.

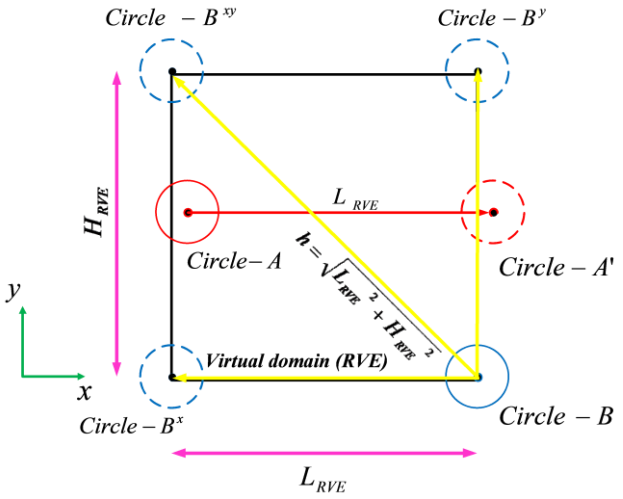

Fig. 3. Representative approach for enforcing the periodicity of material constraints; the circles in dashed lines represent fibres imposed with the constraints.

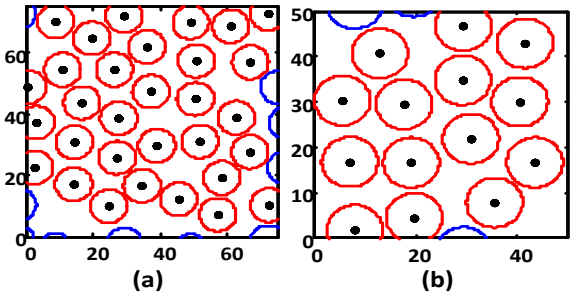

Fig. 4. Representative 2D RVE domains with 53.3% and fibre diameter $11\mu m$: (a) dimension $75 \times 75 units^2$ (b) dimension $50 \times 50 units^2$.1 $unit = 1\mu m$.

2.2. Boundary Conditions

Periodic boundary conditions (PBCs) have been shown to provide more accurate predictions when compared with Dirichlet and/or Neumann boundary conditions [6]. In formulating PBCs for RVEs studied in this work, the conclusions of van der Sluis and associates [9] originally proposed for 2D RVEs have been extended to 3D RVEs here.

2.2.1. Definition of 3D virtual domain

Given a 3D RVE in real space, $\mathbb{R}^3$, with a periodic microstructure, let Ω_{RVE} represent the boundary domain within which the reinforcement and matrix constituents are enclosed as shown in Fig. 6. This domain is cubical of typical dimensions, *a*. The domain Ω_{RVE} comprises six surfaces such that any two surfaces (for example X_{POS} and X_{NEG}) are always parallel to one another in the *x*-, *y*- or *z*-axes. The X_{POS} surface represents the *yz*-plane located at the maximum x-axis cubic dimension (i.e. $x=a$) while its corresponding X_{NEG} surface is located at the minimum *x*-axis cubic dimension (i.e. $x=0$). Each of these surfaces is made up of nodes; hence, for nodes on the X_{POS} surface, they are described as: $X_{POSNodes}$. Similar definitions apply for the remaining five faces. Also for the given domain, *edge nodes* are identified as the set of nodes shared by two intersecting surfaces. If the set of nodes for a given surface is defined as S_{np} where n = *X*, *Y*, *Z* (the reference frames) and p = [POS, NEG] – a collection of all positive or negative faces per given axes; then the set of *surface nodes* for the 3D domain is defined as given in equation 2.

$$S_{\Omega_{RVE}} = \{S_{XPOS} \cup S_{XNEG}\} \cup \{S_{YPOS} \cup S_{YNEG}\} \cup \{S_{ZPOS} \cup S_{ZNEG}\} \quad (2)$$

where $S_{XPOS} \not\subset S_{XNEG}, S_{YPOS} \not\subset S_{YNEG}$ *and* $S_{ZPOS} \not\subset S_{ZNEG}$

2.2.2. Formulation of 3D PBC

In enforcing PBCs for the 3D RVE domain, Ω_{RVE}, all six surfaces and twelve edges of the domain were constrained to undergo synchronous deformation. This condition is satisfied when any pair of surfaces (e.g. S_{XPOS} and S_{XNEG}) is *kinematically tied*. In this study, the formulations for 2D domains proposed by Kouznetsova and associates [10] have been extended to 3D domains. Consider Fig.6, which shows a typical 3D RVE domain, Ω_{RVE}. Let the position vector of any surface node in this domain be $\boldsymbol{U}_i^{S_{np}}$ where S_{np} retains its previous definition and $i=1,\ldots,N$ where N=total number of nodes per surface. Alternatively, let the position vector for any corner node be $\boldsymbol{U}^{N_j}$ where the *corner node* number j = *1,2,…,8.* Four reference nodes are isolated: N_1, N_2, N_3 and N_4 which are called *retained* nodes which will be used to prescribe the required boundary conditions to replicate a desired load case. The remaining corner nodes: N_5 to N_8 and surfaces: $\left(\boldsymbol{U}_i^{S_{xpos}}, \boldsymbol{U}_i^{S_{ypos}}, \boldsymbol{U}_i^{S_{zpos}}\right)$ are called *tied, slave* or *dependent* nodes and surfaces respectively. The *tied* entities are slaves to any displacement or loading on the *retained nodes.* Therefore, the mathematical formulations that prescribe periodic deformation on all nodes bounding Ω_{RVE} are:

$$\boldsymbol{U}_i^{S_{xpos}} - \boldsymbol{U}_i^{S_{xneg}} - \boldsymbol{U}_i^{N_2} + \boldsymbol{U}_i^{N_1} = 0 \quad (3a)$$

$$\boldsymbol{U}_i^{S_{ypos}} - \boldsymbol{U}_i^{S_{yneg}} - \boldsymbol{U}_i^{N_3} + \boldsymbol{U}_i^{N_1} = 0 \quad (3b)$$

$$\boldsymbol{U}_i^{S_{zpos}} - \boldsymbol{U}_i^{S_{zneg}} - \boldsymbol{U}_i^{N_4} + \boldsymbol{U}_i^{N_1} = 0 \quad (3c)$$

In imposing PBC, it is necessary that equilibrium of stresses is satisfied at opposite

edges/surfaces of a given RVE domain [9], [10].

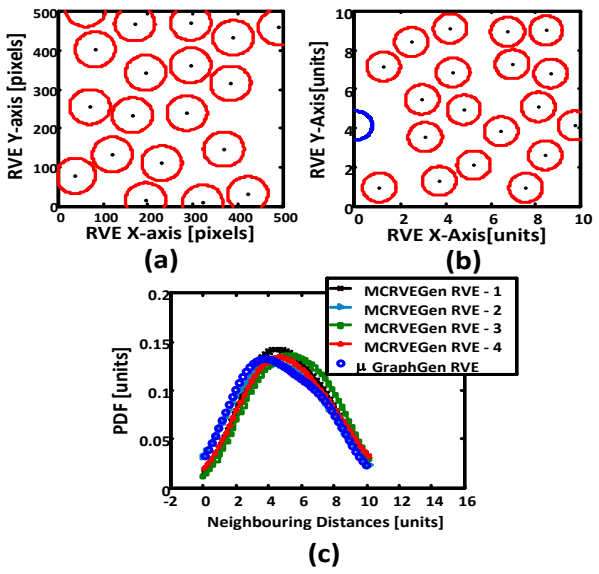

Fig. 5. A comparison of spatial descriptors between a digitized micrograph and numerically derived virtual domains :(a) digitized micrograph from *Plytron*™ ($50\ pixels = 10\mu m = 1\ unit$) (b) typical comparable RVE generated by *MCRVEGen* and (c) comparison of PDFs between the digitized micrograph and four *MCRVEGen*-generated RVEs.

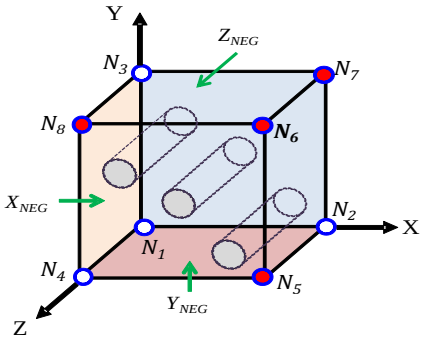

Fig. 6. A typical 3D RVE of a UD reinforced composite showing 8 vertex nodes (N_1 to N_8) and three labelled surfaces (X_{NEG}, Y_{NEG} & Z_{NEG}). The vertices with unfilled circles indicate four retained nodes (N_1 to N_4) whilst the ones with filled circles are 4 slave nodes (N_5 to N_6).

2.2.3. Definition of load cases for 3D RVE

As a consequence of the periodic boundary condition formulation above, where all nodes (except the *retained* nodes) have been kinematically tied, only the *retained nodes* become the material points on which different load cases can be prescribed on the 3D RVE domain, Ω_{RVE}. Therefore, specific constraints have to be imposed on the *retained* nodes in order to create uniaxial and/or shear load cases. The nodal constraints (on the retained nodes) that imposes uniaxial and shear loadings are given in Tables 1 & 2.

2.2.4 The 3D periodic boundary condition generating algorithm (*PBC3DGen*)

In this study, the PBCs were applied as linear constraint equations using the *EQUATION command in ABAQUS™. The task of applying these linear constraints for every pair of nodal sets on all six surfaces and edges is enormous, and doing so manually is onerous. In response, the authors developed an algorithm, *PBC3DGen*: this is a 3D periodic boundary condition generating algorithm for creating linear constraints for every nodal pair of the RVE.

2.3. Computational homogenization

Consider as shown in Fig. 7 a typical test composite enclosed within a macroscale domain, Ω_{MACRO}. Also, assuming statistical homogeneity of the test material, a point within Ω_{MACRO} is defined such that a 3D microscale RVE of the test composite can be isolated and is enclosed in domain, Ω_{RVE}. Let L_{macro} and L_{rve} be the macro and micro lengthscales associated with the two domains. It is to be assumed that the lengthscale of Ω_{MACRO} is many orders of magnitude greater than the lengthscale of Ω_{RVE}, such that $\frac{L_{rve}}{L_{macro}} \ll 1$ for every chosen 3D RVE. Furthermore, if the microscale domain, Ω_{RVE} is imposed with PBCs, the periodically deformed domain can be defined as, $\Omega_{PBC-RVE}$, and this is equivalent to the 3D domain of Fig. 6. The computational homogenization implementation is used here to determine the link between the identified macro- and micro-fields.

Let $\Omega_{PBC-RVE}$ be subjected to a stress tensor, $\boldsymbol{\sigma}$ at a material point, $\mathbf{x}$ within the volume, V enclosed by $\Omega_{PBC-RVE}$, the outward flux of the stress field through a given surface, S_{np} of $\Omega_{PBC-RVE}$ becomes the volume integral of the divergence of the region enclosed by this surface.

$$\int_V \nabla \cdot (\boldsymbol{\sigma} \otimes \mathbf{x})\, dV = \int_V [\mathbf{x} \otimes \nabla \cdot \mathbf{x} + \nabla \mathbf{x}^T \boldsymbol{\sigma}] dV = \int_V \boldsymbol{\sigma} dV \quad (5)$$

Eqn 5 applies when equilibrium of stresses (in the absence of body forces) is assumed since $\nabla \cdot \boldsymbol{\sigma} = 0$ and $\nabla \mathbf{x}^T = \nabla \mathbf{x} = \mathbf{I}$. Re-writing eqn 5 by considering the integral over the surface area, A gives:

$$\int_V \boldsymbol{\sigma} dV = \int_A (\boldsymbol{\sigma} \otimes \mathbf{x}) \cdot \mathbf{n}_{S_{np}} dA = \int_A \mathbf{x} \otimes \mathbf{t}_{S_{np}} dA \quad (6)$$

$\boldsymbol{\sigma}$ is symmetric and surface traction, $\mathbf{t}_{S_{np}} = \boldsymbol{\sigma} \mathbf{n}_{S_{np}}$. Finally, the volume-averaged stress within the

periodically deformed RVE domain, $\Omega_{PBC-RVE}$, shown in Fig. 7. becomes:

$$\langle\boldsymbol{\sigma}\rangle = \frac{1}{V}\int_{\mathrm{V}}\boldsymbol{\sigma}d\mathrm{V} = \frac{1}{V}\int_{A}\mathbf{x}\otimes\mathbf{t}_{S_{np}}d\mathrm{A} \quad (7)$$

where $\langle\boldsymbol{\sigma}\rangle$ is the volume-averaged stress. Since $\Omega_{PBC-RVE}$ is deforming periodically, all tractions on all surfaces vanish during the volume-averaging process leaving only the nodal forces applied to the retained nodes, hence: $\boldsymbol{t}_{S_{np}} = 0$ for surface, S_{np} and

Table 1. Specific nodal constraints imposed on all four retained nodes to create uniaxial deformation along x-, y- or z-axes of the 3D RVE domain.

Node N_1	Node N_2	Node N_3	Node N_4
Uniaxial deformation along x-axis			
$\boldsymbol{U^{N_1}} = \mathbf{0}$	$U_x^{N_2} = \delta_{xx}$	$U_y^{N_3} \neq 0$	$U_z^{N_4} \neq 0$
	$U_y^{N_2} = U_z^{N_2} = 0$	$U_x^{N_3} = U_z^{N_3} = 0$	$U_x^{N_4} = U_y^{N_4} = 0$
Uniaxial deformation along y-axis			
$\boldsymbol{U^{N_1}} = \mathbf{0}$	$U_x^{N_2} \neq 0$	$U_y^{N_3} = \delta_{yy}$	$U_z^{N_4} \neq 0$
	$U_y^{N_2} = U_z^{N_2} = 0$	$U_x^{N_3} = U_z^{N_3} = 0$	$U_x^{N_4} = U_y^{N_4} = 0$
Uniaxial deformation along z-axis			
$\boldsymbol{U^{N_1}} = \mathbf{0}$	$U_x^{N_2} \neq 0$	$U_y^{N_3} \neq 0$	$U_z^{N_4} = \delta_{zz}$
	$U_y^{N_2} = U_z^{N_2} = 0$	$U_x^{N_3} = U_z^{N_3} = 0$	$U_x^{N_4} = U_y^{N_4} = 0$

Table 2. Specific nodal constraints imposed on all four retained nodes to create simple shear deformation on xy-, yz- or xz-planes of the 3D RVE domain.

Node N_1	Node N_2	Node N_3	Node N_4
Simple shear deformation on xy-plane			
$\boldsymbol{U^{N_1}} = \mathbf{0}$	$U_x^{N_2} = U_z^{N_2} = 0$	$U_x^{N_3} = U_y^{N_3} = 0$	$U_x^{N_4} = U_y^{N_4} = 0$
	$U_y^{N_2} = \delta_{xy}$	$U_z^{N_3} = 0$	$U_z^{N_4} = 0$
Simple shear deformation on yz-plane			
$\boldsymbol{U^{N_1}} = \mathbf{0}$	$U_x^{N_2} = U_y^{N_2} = 0$	$U_x^{N_3} = U_y^{N_3} = 0$	$U_x^{N_4} = U_y^{N_4} = 0$
	$U_z^{N_2} = 0$	$U_z^{N_3} = \delta_{yz}$	$U_z^{N_4} = 0$
Simple shear deformation on xz-plane			
$\boldsymbol{U^{N_1}} = \mathbf{0}$	$U_x^{N_2} = U_y^{N_2} = 0$	$U_x^{N_3} = U_y^{N_3} = 0$	$U_x^{N_4} = U_y^{N_4} = 0$
	$U_z^{N_2} = \delta_{xz}$	$U_z^{N_3} = 0$	$U_z^{N_4} = 0$

the retained nodal forces is: $\mathbf{f}_{N_i} \neq 0$ where *i=1,2,…,4* and $\mathbf{x_i}$ is the coordinate position of reference node, N_i. In essence, $\mathbf{f}_{N_i}$ is simply the external force that is applied at the retained nodes, N_i. The volume-averaged stress within the RVE becomes:

$$\langle\boldsymbol{\sigma}\rangle = \frac{1}{V}\left[\mathbf{x}_1\otimes\mathbf{f}_{N_1} + \mathbf{x}_2\otimes\mathbf{f}_{N_2} + \mathbf{x}_3\otimes\mathbf{f}_{N_3} + \mathbf{x}_4\otimes\mathbf{f}_4\right] \quad (8)$$

Eqn 8 represents the volume-averaged stress within $\Omega_{PBC-RVE}$ determined based on virtual work contributions from four retained nodal forces and displacements of the domain[10].

2.4. Prediction of Constitutive Parameters

With the assumption of the global periodicity for $\Omega_{PBC-RVE}$, the overall macroscopic stress is taken to be $\boldsymbol{\sigma}_{macro} = \langle\boldsymbol{\sigma}\rangle$. Similarly, the global strain, $\boldsymbol{\varepsilon}_{macro}$ is calculated from the displacement of the retained nodes given that $\mathbf{u}_1$ = 0 to prevent rigid body motion. Therefore, the individual displacements of the remaining retained nodes become:

$$\mathbf{u}_2 = \boldsymbol{\varepsilon}_{macro}(\mathbf{x}_2 - \mathbf{x}_1),\ \mathbf{u}_3 = \boldsymbol{\varepsilon}_{macro}(\mathbf{x}_3 - \mathbf{x}_1),\ \text{and}\ \mathbf{u}_4 = \boldsymbol{\varepsilon}_{macro}(\mathbf{x}_4 - \mathbf{x}_1) \quad (9)$$

where $\mathbf{u}_2 = \{\mathrm{u}_{i,x}, \mathrm{u}_{i,y}, \mathrm{u}_{i,z}\}$ is the displacement vector of retained node *i* with respect to its coordinate position, $\mathbf{x}_i$.

- *Uniaxial deformation along Z- or 1-axis will result in the following effective properties:*

$$E_{11}^{eff} = \frac{\sigma_{11(macro)}}{\varepsilon_{11(macro)}};\ v_{12}^{eff} = \frac{\varepsilon_{22(macro)}}{\varepsilon_{11(macro)}};\ v_{13}^{eff} = \frac{\varepsilon_{33(macro)}}{\varepsilon_{11(macro)}} \quad (10a)$$

- *Uniaxial deformation along X- or 2-axis will result in the following effective properties:*

$$E_{22}^{eff} = \frac{\sigma_{22(macro)}}{\varepsilon_{22(macro)}};\ v_{21}^{eff} = \frac{\varepsilon_{11(macro)}}{\varepsilon_{22(macro)}};\ v_{23}^{eff} = \frac{\varepsilon_{33(macro)}}{\varepsilon_{22(macro)}} \quad (10b)$$

- *Uniaxial deformation along Y- or 3-axis will result in the following effective properties:*

$$E_{33}^{eff} = \frac{\sigma_{33(macro)}}{\varepsilon_{33(macro)}};\ v_{31}^{eff} = \frac{\varepsilon_{11(macro)}}{\varepsilon_{33(macro)}};\ v_{32}^{eff} = \frac{\varepsilon_{22(macro)}}{\varepsilon_{33(macro)}} \quad (10c)$$

- *Simple Shear deformation along ZX- or 12-, ZY- or 13- and XY- or 23-planes will result in the following shear modulus properties respectively:*

$$G_{12}^{eff} = \frac{\tau_{12(macro)}}{\gamma_{12(macro)}};\ G_{13}^{eff} = \frac{\tau_{13(macro)}}{\gamma_{13(macro)}};\ G_{23}^{eff} = \frac{\tau_{23(macro)}}{\gamma_{23(macro)}} \quad (10d)$$

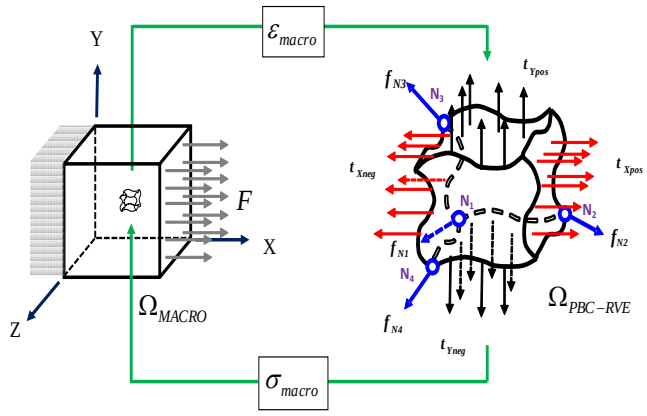

Fig. 7. A 3D representation of macro-to-micro scale transitions for a heterogeneous material.

2.5 Test Materials

Two test materials were used in this work. The first was a boron-aluminium metallic composite with volume fraction 47% [4]. This metallic composite was used to validate predictions from the virtual test-bed proposed in this work. Additionally, it was chosen because of the availability of experimental data on six out of twelve of its elastic constants. Furthermore, Sun and Vaidya [4] published comparisons of several predictive approaches with their approach for the same boron-aluminium composite; hence, this study aimed to rank the current predictions from the virtual test-bed with the entire predictive approaches reported by Sun and Vaidya. The properties of the constituent materials of the boron-aluminium composite are reported in Table 3.

The second test material is an E-glass fibre reinforced polypropylene matrix composite *Plytron*™. This material was used for model predictions and parametric studies (of the validated approach). The properties of the constituents of *Plytron*™ are reported in Table 4.

3. Validation of proposed virtual test-bed

In validating the proposed virtual test-bed, predictions from this study were compared with experiments based on the boron-aluminium composite whose properties are reported in Table 3. In addition, several predictions published in Sun and Vaidya's work [4] and the predictions from this study were compared. Results from these comparisons are shown in Table 5.

The first predictive approach was based on Hashin and Rosen work [11]. It is an analytical approach based on energy variational principles. Sun and Vaidya [4] determined upper and lower bounds of the predicted effective properties using the Hashin-Rosen approach. The lower bounds are the values within the curly brackets in Table 5. The second approach compared is based on Chamis' work [12] which uses a unit cell analytical approach where a square fibre-packing array was assumed, and the RVE divided into several sub-regions. Thirdly, a finite element modelling implementation by Sun and Vaidya [4] was also considered. Sun and Vaidya used two types of 3D RVEs with different deterministic arrangements of fibres: namely, square and hexagonal arrangements. The average state variables within the RVE (i.e. stresses and strains) were obtained using strain energy equivalence principles and Gauss' divergence theorem. Finally, all predictive approaches were compared against actual experimental data of the boron-aluminium composite obtained by Kenaga and associates [13].

In this study, two different 3D RVE types were used: (a) *FEM small*: a 3D RVE of typical dimensions, 30μm, with a single fibre inclusion and (b) *FEM big*: a 3D RVE of typical dimensions, 100μm with 27 fibres (being a statistically representative RVE of the test composite). The RVE size for *FEM Big* was chosen to ensure convergence of predicted elastic properties (see section 4.1); also, both 3DRVE types had sufficient mesh density to ensure convergence (see section 4.5). In all cases, the volume fraction of, 47% remained constant. The *FEM small* was adopted as a direct comparison to Sun and Vaidya's model [4] whilst the *FEM big* was chosen to assess if the virtual test-bed proposed in this study had any advantages over the other approaches.

In general, the predictions from this study, Sun, and Hashin agree well with those from experiments. However, predictions of the shear modulus G_{12} and the transverse modulus E_{22} based on Chamis' work were slightly higher than the experimental data as well as other predictive approaches. A probable reason for this is the improperly chosen boundary conditions. Finally, the framework presented in this study is the only approach that predicted all the possible effective elastic properties of the composite because a statistically representative 3D RVE was used in conjunction with appropriate boundary conditions. The virtual test-bed gives the closest predictions to experimental data for the given elastic constants of the test composite. Therefore, this virtual test-bed is most suited for use as a predictive approach for determining a holistic range of effective elastic properties of UD composites. The predictions obtained from the two RVE types

considered here in this work show results from *FEM Small* were, in some cases (e.g. E_{22}), higher compared to that of the *FEM big*. One probable reason for this disparity is that *FEM small* lacks sufficient fibres for it to be regarded as being statistically representative of the test composite; hence, the possibility for it to produce non-representative predictions.

Table 3. Properties of the constituents of Boron-Aluminium composite (V_f = 47%) [4].

Material	Young's modulus (GPa)	Poisson's ratio, $\boldsymbol{\nu}$
Boron	379.3	0.1
Aluminium	68.3	0.3

Table 4. Properties of constituents for *Plytron*™ composite [14], [15]

Material	Young's modulus(GPa)	Poisson's ratio, $\boldsymbol{\nu}$
Glass fibre	73	0.20
Polypropylene	1.308	0.43

4. Results and discussion

4.1. Critical RVE size, $L_{RVE,crit}$

Before any characterization of a material's response can be accomplished using micro-mechanical analysis, an appropriately sized RVE must be isolated from the parent material first [6]. An appropriately sized RVE is attained when the magnitude of any predicted material property obtained using the RVE is invariant with any further increases in size of that RVE. In order to determine an appropriate size of the generated RVEs for the chosen test material (in this case *Plytron*™), a geometric parameter, λ, was defined as the ratio of the fibre reinforcement, $\emptyset_i$, and the characteristic length of any side of an RVE cube, L_{RVE}: $\lambda = \frac{L_{RVE}}{\emptyset_i}$. The diameter of the fibre of *Plytron*™ was determined from a digitized micrograph to be approximately 15μm. The geometric parameter, λ, was varied between 1.5-10 to establish convergence of all possible predicted elastic properties.

In all simulations, the volume fraction and diameter of the inclusions remained constant at 35% and 15μm respectively. Results from these simulations are reported in Figs. 8-9. These results show a critical RVE, $L_{RVE,crit}$ exists for $\lambda \geq 6.0$ beyond which, there was no appreciable change in all predicted properties. All RVEs used in subsequent simulations satisfied this geometric parameter criterion.

4.2. Effect of different spatial realizations

Table 6 shows the longitudinal elastic modulus, E_{11} is insensitive to spatial realization of inclusions hence the low standard deviation. However, the high standard deviation for the transverse moduli (E_{22} and E_{33}) reflects a higher sensitivity to spatial realization. Consequently, the transverse Poisson ratios (ν_{23}&ν_{23}) show significant variability unlike the longitudinal Poisson ratios, (ν_{12}&ν_{13}). Also, the shear moduli were highly dependent on spatial realizations since the shear load cases involve the displacement of inclusions from their original positions through a sliding/rolling motion.

4.3. Comparison of different Approaches

The virtual framework developed in this study was used to determine effective properties for *Plytron*™ but for varying volume fractions. Predictions were compared against experimental data obtained for *Plytron*™ and other analytical and/or semi-analytical approaches. The approaches considered include: (a) *Rule of mixtures - ROM* (b) *Hopkins-Chamis square array method* and (c) *Halpin-Tsai semi-empirical method.* Experimental data for *Plytron*™ with volume fraction of 35% were derived from [14]. In the longitudinal direction, the results showed a linear relationship between increase in the volume fraction of reinforcements and the predicted modulus and Poisson ratios. However, the dependence of E_{22} and G_{12} on increased volume fraction was non-linear. Above all, the results shown in Fig. 10 & Fig 15 indicate the virtual test-bed predictions gave the closest values to experiments.

4.4. Effect of boundary condition types on predicted effective properties

An RVE which is representative of its parent material should ideally produce results invariant of the imposed boundary conditions (BCs) [9]. However, for this universal condition to hold, the size of the RVE has to be extremely large, making it unfeasible to simulate efficiently given limited computing resources. Therefore, this study aims to quantify the effect of several boundary condition types on the predicted effective properties for *Plytron*™ . Three types of commonly used boundary conditions were considered: (a) *Dirichlet*, (b) *Neumann* and (c) *periodic boundary conditions.*

Results from uniaxial and shear simulations using cubic RVEs are shown in Fig. 11-12. It is well reported in the literature that predictions based on Dirichlet BCs and Neumann BCs overestimate and underestimate effective properties respectively [9]. As a result, predictions using periodic BCs are bounded by those of the Dirichlet and Neumann BCs. This conclusion is confirmed in Fig. 11*a* for the longitudinal modulus, E_{11} but not for the *transverse* and *shear moduli* as well as *Poisson ratios* where the periodic boundary condition gave the least predicted effective properties. It seems the generally accepted conclusions of effective properties based on periodic BCs to be bounded by those of Neumann and Dirichlet BCs is partially valid. This study has observed and therefore concludes that if the dependence of effective properties on volume fraction follows a nonlinear relationship, the periodic BCs give the least predicted effective properties. This is confirmed in Fig. 11b-12b except for Fig. 12c where the periodic BCs gave the highest effective properties. The effect of boundary conditions for these cases is minimal when periodic BCs are used. However, further studies need to be done to conclusively show the effect of boundary conditions on predicted effective properties.

Table 5. Comparison of predicted effective elastic properties of boron-aluminium $(V_{frac} = 47\%)$ obtained using different approaches. Note: the fibre direction is along the 1-axis.

Elastic Constants(GPa)	Experiment[a]	FEM small[b]	FEM big[c]	FEM Sun [d] (Square /Hexagonal)	Analytical[e]	Semi-empirical[f]
E_{11}	216	215	214	215 / 215	215	214
E_{22}	140	141	134	144 / 136.5	139.1{131.4}	156
E_{33}	-	141	135	-	-	-
v_{12}	0.29	0. 195	0. 196	0.19 / 0.19	0.195	0.20
v_{13}	-	0.195	0.194	-	-	-
v_{23}	-	0. 255	0. 302	0.29 / 0.34	0.31 {0.28}	0.31
G_{12}	52	51.9	52.0	57.2 / 54.0	53.9	62.6
G_{13}	-	52.0	52.8	-	-	-
G_{23}	-	45.0	49.4	45.9 / 52.5	54.6 {50.0}	43.6

Key to table:

[a] Experiment: Experimental data of boron-aluminium composites from work of Kenaga, *et. al.*
[b] FEM Small: FEM based on this study using a Small RVE with window size 30μm^2 and 1 fibre.
[c] FEM Big: FEM based on this study using a Big RVE with window size 100μm^2 and 27 fibres.
[d] FEM Sun: FEM approach due to the work of Sun and Vaidya for square and hexagonal arrays.
[e] Analytical: Analytical approach based on energy-balance principles of Hashin and Rosen.
[f] Semi-Empirical: Semi-empirical approach proposed by Chamis.

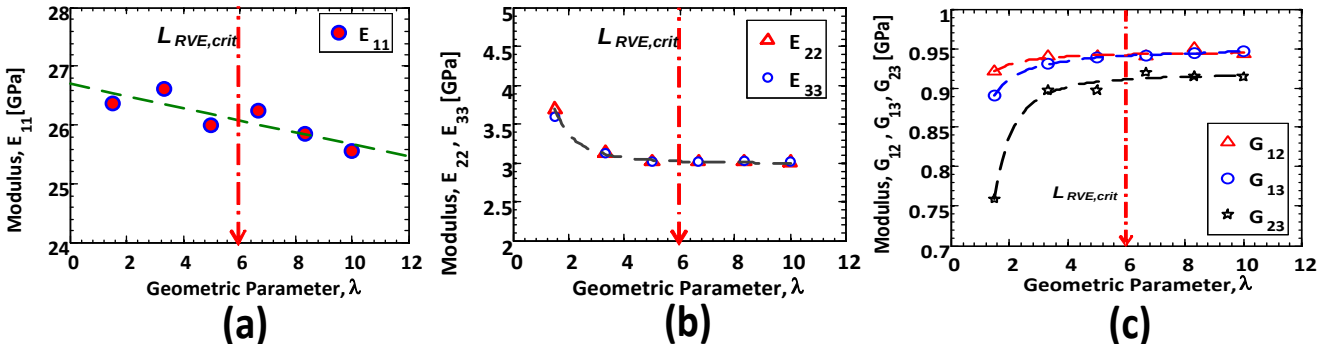

Fig. 8. Variation of predicted effective properties with increasing geometric parameter, λ (a) longitudinal Young's modulus E_{11} (b) transverse moduli E_{22} & E_{33} and (c) Shear Moduli G_{12}, G_{13} & G_{23}.

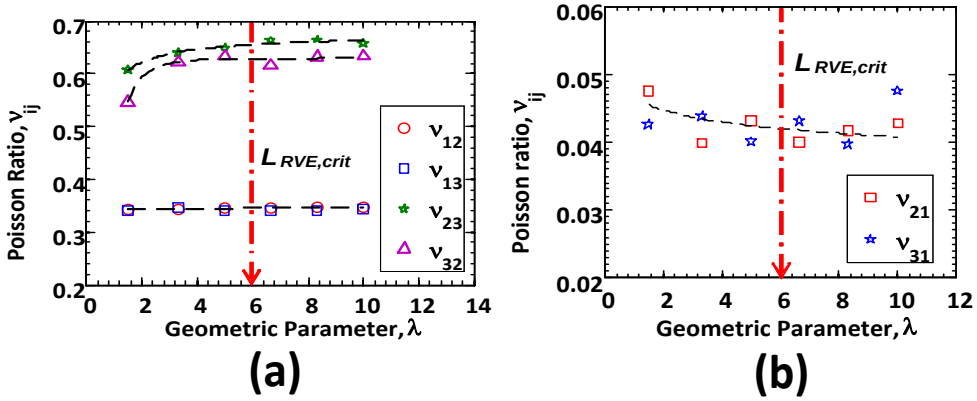

Fig. 9. Variation of predicted Poisson ratios ν_{12} with increasing geometric parameter λ.

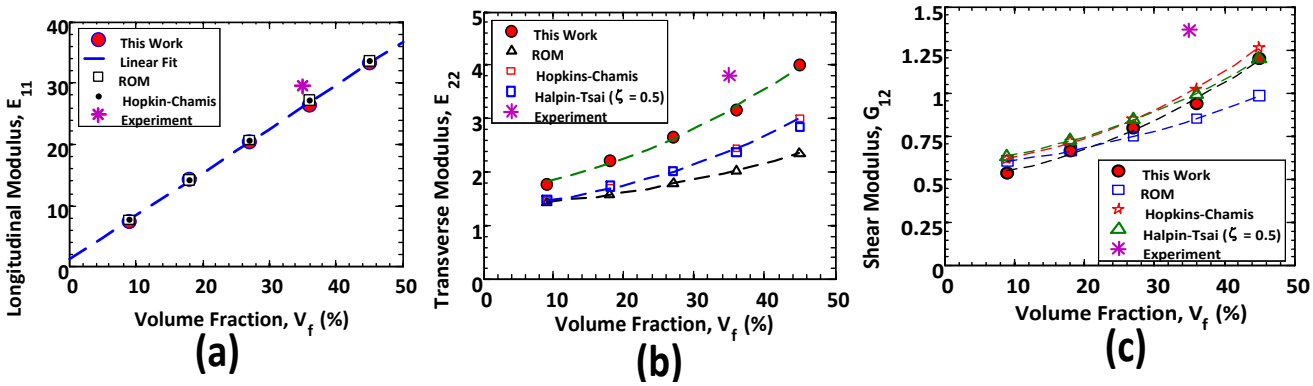

Fig. 10. Comparison of predicted effective elastic constants between this work and other approaches (a) longitudinal Young's modulus E_{11} (b) transverse modulus E_{22} (c) shear modulus, G_{12}

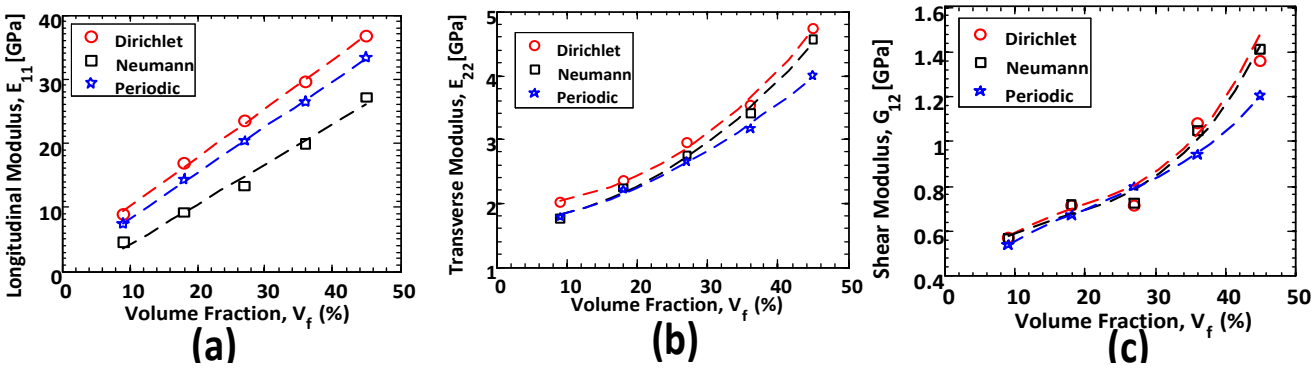

Fig. 11. Effect of boundary condition types on predicted effective elastic properties (a) longitudinal modulus, E_{11} (b) transverse modulus, E_{22} (c) major shear modulus G_{12}.

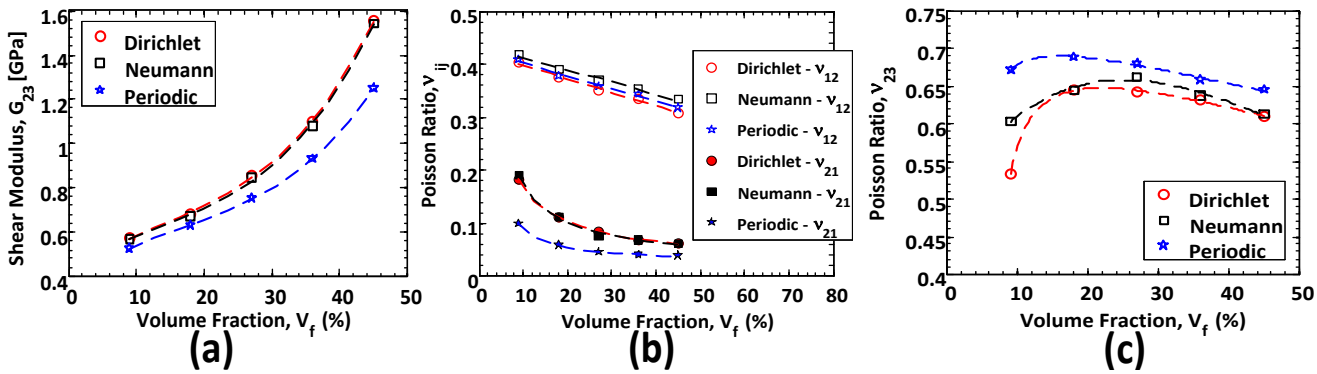

Fig. 12. Effect of boundary condition types on predicted effective elastic properties (a) minor shear modulus G_{23}. (b) major and minor Poisson ratios, ν_{12} & ν_{21} (c) minor Poisson ratio ν_{23}.

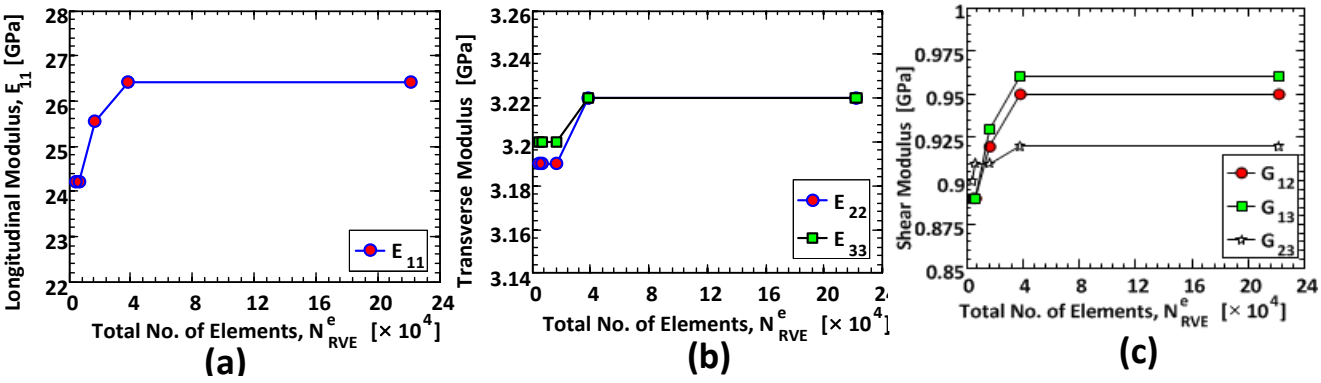

Fig. 13. Effect of mesh sensitivity on predicted effective elastic properties (a) longitudinal modulus, E_{11}. (b) transverse moduli, E_{22} & E_{33} (c) shear moduli G_{12}, G_{13} & G_{23}

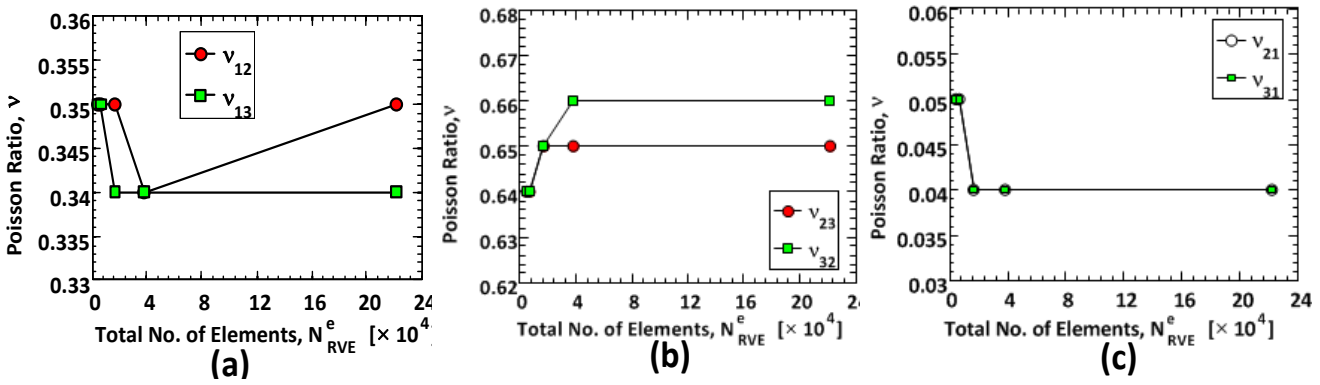

Fig. 14. Effect of mesh sensitivity on predicted effective elastic properties (a) longitudinal modulus, E_{11}. (b) transverse moduli, E_{22} & E_{33} (c) shear moduli G_{12}, G_{13} & G_{23}

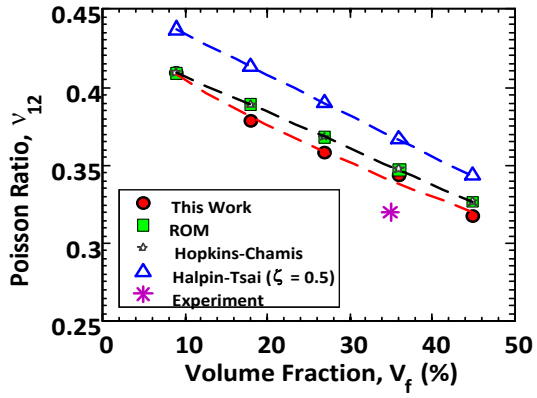

Fig. 15 Comparison of Poisson ratio, v_{12} determined in this work with predictions based on other approaches.

4.5. Mesh sensitivity study on effective properties

In this section, the mesh density sensitivity of the virtual test-bed in predicting effective properties for *Plytron*™ was assessed. Five mesh densities ranging from 4584 elements to 221696 elements were sampled. Plots of effective properties of interest against total number of elements, N^e_{RVE} were determined. The results of the mesh sensitivity convergence profile for all twelve elastic constants are given in Fig. 13-14. According to Fig. 13-14, all effective properties converged at a mesh density of about 40,000 elements. For a 3D RVE of typical edge length, L_{RVE} = 30μm, the above mesh density represents an edge discretization of at most 2μm.

Table 6. Effect of spatial realizations on predicted effective properties. NB: Units of moduli, E_{ij} and G_{ij} is in *GPa* where i,j = 1,2,3.

Elastic constants	Mean	Standard deviation
E_{11}	25.86	0.030
E_{22}	3.16	0.110
E_{33}	3.18	0.090
G_{12}	0.93	0.010
G_{13}	0.94	0.020
G_{23}	0.93	0.020
v_{12}	0.345	0.004
v_{13}	0.342	0.004
E_{23}	0.656	0.010
G_{21}	0.042	0.001
G_{31}	0.042	0.001
G_{32}	0.659	0.013

5. Conclusions

This study developed a virtual test-bed for predicting a holistic range of elastic properties of a typical UD composite material. The virtual framework is based on 3D RVEs which comprises the following; (a) the geometrical modelling of statistically representative RVEs (b) prescription of appropriate PBCs for desired load cases and application of a robust macro-micro homogenization scheme to predict effective elastic constants. Several statistical-numerical modules were incorporated in various frames of the test-bed to either corroborate numerically derived parameters with experimental data, or ensure strict virtual domain objectivity. The test-bed predicted the entire set of effective elastic constants with excellent accuracy compared to other existing approaches. Furthermore, unlike other comparable approaches, this test-bed requires no a priori assumptions about material constitutive response along any material axis. Therefore, with adequate extensions (i.e. incorporating robust micro-scale material models), the presented virtual test-bed is suitable for investigating nonlinear responses of UD composites.

References

[1] D. Trias, J. Costa, J. a. Mayugo, and J. E. Hurtado, "Random models versus periodic models for fibre reinforced composites," *Computational Materials Science*, vol. 38, no. 2, pp. 316–324, Dec. 2006.

[2] M.-J. Pindera, H. Khatam, A. S. Drago, and Y. Bansal, "Micromechanics of spatially uniform heterogeneous media: A critical review and emerging approaches," *Composites Part B: Engineering*, vol. 40, no. 5, pp. 349–378, Jul. 2009.

[3] R. Krueger, I. L. Paris, T. Kevin O'Brien, and P. J. Minguet, "Comparison of 2D finite element modeling assumptions with results from 3D analysis for composite skin-stiffener debonding," *Composite Structures*, vol. 57, no. 1–4, pp. 161–168, Jul. 2002.

[4] C. T. Sun and R. S. Vaidya, "Prediction of composite properties from a representative volume element," *Composites Science and Technology*, vol. 56, no. 2, pp. 171–179, 1996.

[5] a. R. Melro, P. P. Camanho, and S. T. Pinho, "Influence of geometrical parameters on the elastic response of unidirectional composite materials," *Composite Structures*, vol. 94, no. 11, pp. 3223–3231, Nov. 2012.

[6] I. M. Gitman, H. Askes, and L. J. Sluys, "Representative volume: Existence and size determination," *Engineering Fracture Mechanics*, vol. 74, no. 16, pp. 2518–2534, Nov. 2007.

[7] V. a. Buryachenko, N. J. Pagano, R. Y. Kim, and J. E. Spowart, "Quantitative description and numerical simulation of random microstructures of composites and their effective elastic moduli," *International Journal of Solids and Structures*, vol. 40, no. 1, pp. 47–72, Jan. 2003.

[8] a Melro, P. Camanho, and S. Pinho, "Generation of random distribution of fibres in long-fibre reinforced composites," *Composites Science and Technology*, vol. 68, no. 9, pp. 2092–2102, Jul. 2008.

[9] O. Van Der Sluis, P. J. G. Schreurs, W. A. M. Brekelmans, and H. E. H. Meijer, "Overall behaviour of heterogeneous elastoviscoplastic materials : effect of microstructural modelling," *Science*, vol. 32, pp. 449–462, 2000.

[10] V. Kouznetsova, W. A. M. Brekelmans, and F. P. T. Baaijens, "An approach to micro-macro modeling of heterogeneous materials," *Computational Mechanics*, vol. 27, no. July 2001, pp. 37–48, 2001.

[11] Z. Hashin and B. W. Rosen, "The elastic moduli of fibre-reinforced materials," *Journal of Applied Mechanics, Transactions ASME*, vol. 31, pp. 223–232, 1964.

[12] Christos C. Chamis, "Simplified composite micromechanics equation for hygral, thermal, and mechanical properties," *S.A.M.P.E. quaterly*, vol. 153, pp. 14–23, 1984.

[13] D. Kenaga, J. E. Doyle, and C. T. Sun, "The characterization of boron/aluminium composite in the nonlinear range as an orthotropic elastic-plastic material," *Journal of Composite Materials*, vol. 21, no. 6, pp. 516–531, 1987.

[14] M. I. Okereke, C. P. Buckley, and C. R. Siviour, "Compression of polypropylene across a wide range of strain rates," *Mechanics of Time-Dependent Materials*, vol. 16, no. 4, pp. 361–379, Jan. 2012.

[15] M. I. Okereke and A. I. Akpoyomare, "A virtual framework for prediction of full-field elastic response of unidirectional composites," *Computational Materials Science*, vol. 70, no. null, pp. 82–99, Apr. 2013.